**Proceedings of ASME Turbo Expo 2011**
**GT2011**
**June 6-10, 2011, Vancouver, British Columbia, Canada**

# GT2011-46479

# INVESTIGATIONS OF SECONDARY FLOW SUCTION IN A HIGH SPEED COMPRESSOR CASCADE

**Christoph Gmelin**[*]
**Frank Thiele**
Department of Fluid Mechanics and Engineering Acoustics
Berlin Institute of Technology (TUB)
Müller-Breslau-Straße 12
10623 Berlin, Germany
Email: christoph.gmelin@cfd.tu-berlin.de

**Karsten Liesner,**
**Robert Meyer**
Institute of Propulsion Technology
German Aerospace Center (DLR)
Müller-Breslau-Straße 8
10623 Berlin, Germany
Email: karsten.liesner@dlr.de

## ABSTRACT

*Numerical and experimental results for a high-speed compressor cascade with secondary flow suction are presented. Steady flow suction of low momentum fluid from the back flow region in the corner between end wall and vane is considered in order to diminish the corner separation. Investigations are performed at the design point with an inlet Mach number of 0.67 and a Reynolds number of 560,000 based on axial chord and inlet velocity. The steady Reynolds-Averaged Navier-Stokes simulations are evaluated against data from the accompanying experiment collected with pitot tubes and Conrad angle probes. Laminar separation bubbles on both suction and pressure surface are observed. Thus, transition from laminar to turbulent flow is respected in the simulations. The uncontrolled base flow case and various suction ratios (ratio of drawn to passage mass flow) are exploited. Additionally, the position of the slot is varied numerically. It is found that relocation of the slot slightly away from the suction surface improves the performance of the flow suction.*

## NOMENCLATURE

### Geometric Parameters

| | | |
|---|---|---|
| $c$ | m | vane chord |
| $s$ | m | vane span |
| $t$ | m | cascade pitch |
| $x, y, z$ | m | coordinate system |
| $\alpha$ | deg | flow angles |

### Flow Quantities

| | | |
|---|---|---|
| $Ma$ | 1 | Mach number |
| $p$, $p_t$, $q$ | Pa | static, total, dynamic pressure |
| $Re$ | 1 | Reynolds number |
| $V$ | $m/\mathrm{s}$ | velocity |
| $y^+$ | 1 | dimensionless wall distance |
| $\delta_{99}$ | m | boundary layer thickness |
| $\Delta p/q_1$ | 1 | static pressure rise |
| $\nu_{(t)}$ | $m^2/\mathrm{s}$ | (turbulent) kinematic viscosity |
| $\omega$ | $1/\mathrm{s}$ | vorticity |
| $\zeta_{q_1}$ | 1 | total pressure loss coefficient |
| $\rho$ | $kg/\mathrm{m}^3$ | density |
| $\tau_w$ | Pa | wall shear stress |

### Subscripts

| | |
|---|---|
| *base* | base flow |
| *exp* | experiment |
| *s* | stagger |
| *sim* | simulation |
| *suct* | suction |
| $x, y, z$ | component in x,y,z direction |
| 1, 2 | inlet, outlet |

[*] Address all correspondence to this author.

## INTRODUCTION

Modern compressor stages have to meet high design criteria. For safety reasons, instabilities like stall and surge have to be avoided, which is why the stage load is limited and today's engines have a multitude of compressor stages. In order to reduce the number of stages, the pressure rise per stage needs to be maximized. Thus, engines could be built more compact, lighter, and more efficient [1]. These days, compressor stages therefore comprise a number of passive flow control devices including blade sweep [2], three-dimensional airfoil designs [3], and vortex generators at the side walls [4]. Recently, *active* flow control concepts are considered in turbomachinery application to further increase the stage load or extend the operating range of the engine. Lord et al. [5] give an overview of flow control opportunities in gas turbine engines.

The better understanding of compressor aerodynamics is investigated in linear compressor cascades since the 1950's [6], [7]. In the following decades, the involved secondary flow phenomena and their influence on the cascade losses have been analyzed [8], [9] and still are today [10]. The idea of increasing the compressor efficiency by influencing the secondary flow by means of flow control is similarly old [11], [12]. Already in 1965, Peacock [13] was able to eliminate the corner separation by boundary-layer suction at the side walls in a low-speed compressor cascade. Based on these results, the control of corner separation by slot suction is investigated in a high-speed compressor cascade. Improving the compressor performance via flow suction represents a lucrative way to use the bleed air drawn from the stage anyway.

The work presents numerical investigations performed by means of steady Reynolds-Averaged Navier-Stokes (RANS) simulations at the Department of Fluid Mechanics and Engineering Acoustics of the Berlin Institute of Technology (TUB). Since Computational Fluid Dynamics (CFD) has become a helpful tool within the industrial design process of turbomachinery blades, the possibility of determining the impact of flow control concepts over night represents an important first step toward their final realization in the engine. The experimental work is performed by the German Aerospace Center (DLR) at the Institute of Propulsion Technology in Berlin, Germany, where various passive [4] and active [14] flow control methods have been investigated in a high-speed wind tunnel.

Within the frame of the present paper, numerical and experimental results of a high-speed compressor cascade are presented. The investigations include evaluation of the unforced base flow and cases with secondary flow suction through slots in the side walls. Considering various suction ratios, i.e. the ratio of drawn to passage mass flow, reveals that the impact of secondary flow suction is mainly driven by the magnitude of the drawn mass flow. Simulations of different suction slot positions show that beneficial control locations can be determined numerically.

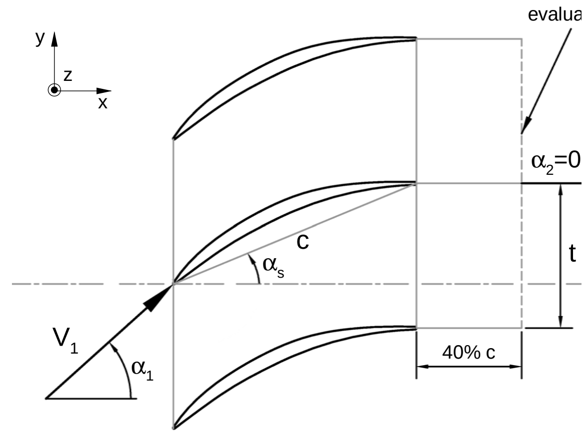


**FIGURE 1**. OVERVIEW OF THE STATOR CASCADE WITH DEFINITION OF GEOMETRIC PARAMETERS.

## CASCADE AERODYNAMICS

The linear compressor cascade configuration under investigation consists of NACA 65-K48 profiles, which represent an established geometry still in use and continued to be used. At the design point, the inflow angle is $\alpha_1 = 42°$ and the turning is $\Delta\alpha = 42°$, resulting in an outflow angle of $\alpha_2 = 0°$. The design Mach number at the inflow is $Ma_1 = 0.67$ which results in a Reynolds number of $Re_c = 560,000$ based on $c = 0.04$m axial chord. The aspect ratio of the vanes is $s/c = 1$ and the pitch to chord ratio of the cascade is $t/c = 0.55$. The stagger angle is $\alpha_s = 22.5°$. An overview of the stator cascade is shown in Fig. 1 and the geometrical parameters are summarized in Tab. 1.

For the design point, the experimentally observed de Haller coefficient is $(V_2/V_1)_{exp} = 0.81$ and the axial velocity density ratio is measured to $AVDR_{exp} = 1.1$. Due to discrepancies in static pressure rise, the values of the simulation differ slightly. The numerical values are $(V_2/V_1)_{sim} = 0.75$ and $AVDR_{sim} = 1.06$.

**TABLE 1**. CASCADE AND BLADE GEOMETRY DATA.

| Parameter | Variable | Value | Unit |
|---|---|---|---|
| Chord length | $c$ | 0.04 | m |
| Blade span | $s$ | 0.04 | m |
| Blade pitch | $t$ | 0.022 | m |
| Aspect ratio | $s/c$ | 1 | 1 |
| Pitch to chord | $t/c$ | 0.55 | 1 |
| Inflow angle | $\alpha_1$ | 42 | deg |
| Stagger angle | $\alpha_s$ | 22.5 | deg |

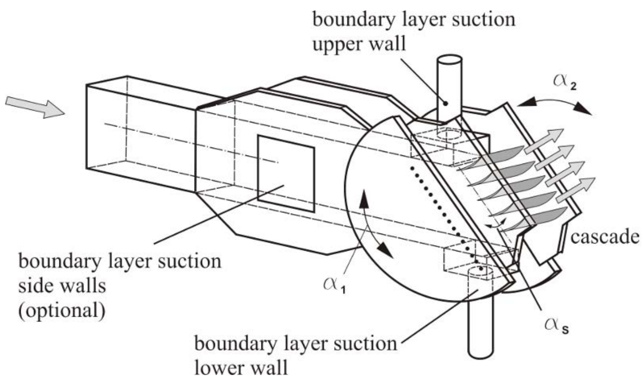


**FIGURE 2**. OVERVIEW OF THE CASCADE TEST FACILITY.

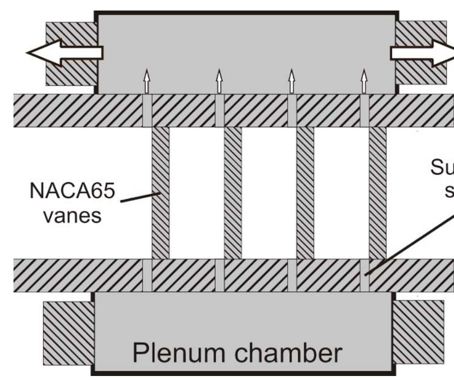


**FIGURE 3**. SKETCH OF THE EXPERIMENTAL SETUP OF THE SECONDARY FLOW SUCTION.

## EXPERIMENTS

The test rig of the high-speed wind tunnel is shown in Fig. 2. Upstream of the cascade, a settling chamber with 1m diameter is installed where the flow is decelerated to velocities below $V = 1{}^{m}\!/\!{}_{s}$. The adjacent nozzle has a contraction ratio of $1:218$ and accelerates the flow up to a Mach number of $Ma = 0.7$. Thus, Reynolds numbers of $Re = 600,000$ can be investigated. Downstream of the nozzle, at the cascade inlet, the rectangular cross section has a width of 0.04m (equal to span) and a height of 0.09m (equal to four times pitch). The boundary layer height of each wall can be controlled independently by suction. The upper and lower boundary layer thickness are adjusted to ensure periodic inflow conditions which are monitored by a row of static pressure probes. The performance of the cascade is evaluated using total pressure measurements in the wake. The inflow angle can be adjusted geometrically from 32° to 56°. A detailed description of the wind tunnel and the measurement procedures can be found in [15].

### Measurement Techniques

The wake measurements are performed using a wake rake consisting of 26 pitot tubes. The rake is traversed in pitch-wise direction on a plane 0.016m (40% of the chord length) downstream of the trailing edge. Hereby, the 26 tubes are distributed from 2.5% span to 97.5% span and hold an outer diameter of only $0.7 \cdot 10^{-3}$m. The total pressure values are measured in a multi-channel pressure transducer with an accuracy of $\pm 0.05\%$ of the full-scale measurement range, i.e. $\pm 17$Pa. Previous investigations have shown that there is no upstream influence of the rake on the cascade flow. For outflow angle determination a set of four Conrad angle probes with an opening angle of 90° is traversed on the same measurement plane. The boundary layer thickness at the side walls is measured with a six tube boundary layer probe upstream of the cascade. In order to provide a numerical boundary condition, the total pressure profile of the incoming flow has been measured with a flattened pitot probe at the inlet of the computational domain.

### End Wall Suction

The secondary flow suction through the cascade end walls is realized with a side channel blower (compressor) providing 3,500W. Within the 0.01m thick side walls, the slots are quasi two-dimensional. They end up into a plenum chamber mounted onto each of the end walls (cf. Fig 3). These 0.1m x 0.02m x 0.02m large plenum chambers are evacuated by the compressor through large diameter tubes. Since the plenum chambers are large compared to the suction slots, the flow is assumed to be evenly distributed between the slots. The suction mass flow is monitored in the tubes using a Venturi meter.

## NUMERICS

For the numerical investigations, the flow solver *ELAN3D* [16], developed at the Institute of Fluid Mechanics and Engineering Acoustics of the Berlin Institute of Technology, is used. The utilized meshes are created with *G3DMESH* [17], a tool developed at the German Aerospace Center in Cologne especially for turbomachinery applications.

### Flow Solver

*ELAN3D* is an implicit, pressure based flow solver of finite volume kind, providing a fully conservative approximation of the governing equations formulated on curvilinear coordinates. Due to the high Mach number of the cascade flow, all simulations are performed solving the compressible RANS equations.

Continuity and momentum equation are connected using a SIMPLE-type pressure correction algorithm in combination with a generalized Rhie & Chow interpolation [18] to prevent pressure and velocity fields from decoupling. The code is based on a cell-centered, co-located storage arrangement on semi block-structured grids and delivers second order accuracy in space and time. Parallelization is implemented via domain decomposition and the data interchange between separated domains is realized using standardized MPI-libraries.

For turbulence closure, the Menter SST-k-$\omega$ [19] model is chosen because of its strong reliability in the prediction of separation in the presence of adverse pressure gradients. Transition positions at both suction and pressure side are fixed using a step function to trigger the production term of the turbulence model. The production is zero within the laminar regime. At an axial position that delivers best accordance with the experimental results, the turbulent production is enabled along the span. For the design point, transition is triggered at 55% chord for the suction side and 0.6% chord on the pressure side of the blade. The side walls are treated fully turbulent.

### Computational Domain

According to the flow solver and the applied low Reynolds turbulence model, the mesh is block structured and approximately 33 grid points resolve the boundary layer down to the viscous sublayer in wall normal direction ensuring a dimensionless wall distance of $y^+ \approx \mathcal{O}(1)$.

Due to symmetry reasons and the steady treatment of the flow, only half of the span is considered within the simulations. Preliminary investigations revealed that the use of 1.23 million control volumes ensures sufficient resolution of the secondary flow phenomena. The used mesh resolves the half span with 65 and the pitch with 79 grid points. Around the vane, 201 points are distributed. The resulting mesh is depicted in Fig. 4 showing every second grid point on the blade and end wall surfaces, as well as the distribution of the dimensionless wall distance. The maximum value is $y^+_{max} = 1.77$.

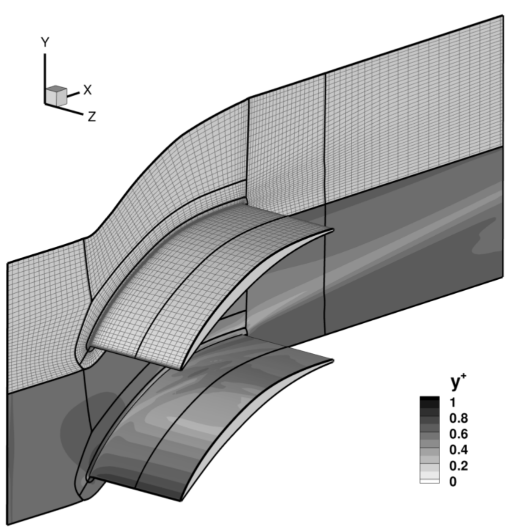


**FIGURE 4**. OVERVIEW OF THE COMPUTATIONAL DOMAIN SHOWING EVERY SECOND GRID POINT ONLY AND DISTRIBUTION OF DIMENSIONLESS WALL DISTANCE.

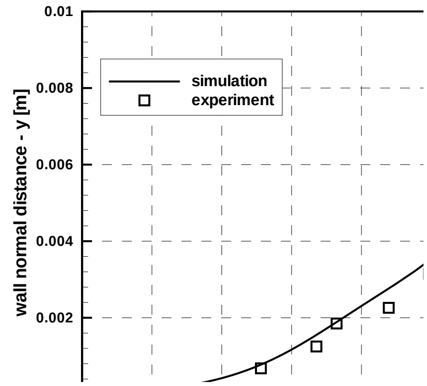


**FIGURE 5**. EVALUATION OF THE INCOMING BOUNDARY LAYER FOR THE DESIGN POINT.

### Boundary Conditions

During preparatory simulations, a strong influence of the incoming boundary layer thickness on the secondary flow and thus the losses of the cascade was observed. In order to account for the boundary layer measured in the experiment, profiles of all flow and turbulence variables used as inlet boundary conditions are extracted from a separately performed flat plate simulation. The simulated boundary layer is compared to the measurement in Fig. 5 by means of the toal pressure $p_t$. The boundary layer thickness at the side wall is measured at a plane corresponding to the inlet of the computational domain of the cascade. The value of $\delta_{99} = 4$mm (i.e. 10% of the span) is well represented by the flat plate simulation.

In addition to the total pressure, profiles of velocity and temperature are extracted from the flat plate simulation and imposed as boundary conditions at the inlet in order to achieve the desired inflow Mach number at the corresponding Reynolds number. The experimentally measured turbulence intensity of $Tu = 4\%$ has been respected in the flat plate simulation and a, for turbomachinery application commonly used, eddy viscosity ratio of ${}^{\nu_t}/_{\nu} = 5$ is assumed in the free stream outside of the boundary layer. Thus, the turbulent production and dissipation, extracted from the flat plate simulation, represent the experimental flow conditions as good as possible.

## DATA EVALUATION

The prediction of the simulation and the experimentally measured data are compared by calculating classical cascade parameters, i.e. the total pressure loss coefficient $\zeta_{q_1}$ as defined in Eq. 1 and the static pressure rise ${}^{\Delta p}/_{q_1}$ as defined in Eq. 2. Subscript "1" indicates the inlet evaluation plane which corresponds to the inlet of the computational domain of the cascade. Subscript "2" indicates the outlet evaluation plane, located at 40%

axial chord downstream of the trailing edge (cf. Fig. 1), corresponding to the measurement plane in the experiment.

$$\zeta_{q_1} = \frac{p_{t,1} - p_{t,2}}{q_1} \tag{1}$$

$$\frac{\Delta p}{q_1} = \frac{p_2 - p_1}{q_1} \tag{2}$$

Another parameter representative for the performance of a compressor stage is the achieved turning $\Delta\alpha$ of the flow or simply the outflow angle $\alpha_2$ at the measurement plane.

These parameters are averaged in pitch-wise direction in order to evaluate values only dependent on the position along the blade span and the distance of the evaluation plane. Hereby, the total pressure loss and the outflow angle are mass-averaged, whilst the pressure rise is area-averaged over the passage. By further integrating these pitch-averaged values over the span, integral averaged values are calculated defining the cascade performance by single numbers. This procedure is beneficial in order to evaluate the cases with secondary flow suction since forcing of the flow can lead to considerable redistributions of the three-dimensional flow.

## RESULTS

In the following the results of the unforced base flow at the design point are discussed and the simulation is evaluated against experimental data. Numerical and experimental investigations with secondary flow suction are presented for various suction mass flow ratios. The following variation of the suction slot position is performed in the simulations only.

### Base Flow

At first, the design point of the blade ($Ma_1 = 0.67$, $Re_c = 560{,}000$, $\alpha_1 = 42°$) is simulated. Sufficient convergence is reached within 20,000 iterations, corresponding to a wall clock time of approximately 12 hours running the computation in parallel mode on 8 CPUs with 2.4 GHz.

The secondary flow structures evolving within the passage are identified using isosurfaces of the $\lambda_2$-criterion introduced by Jeong and Hussain [20]. In Fig. 6, the $\lambda_2 = -10^7$-isosurfaces are color-coded with the local value of the axial vorticity $\omega_x$. The view is from downstream into the cascade onto the trailing edge and for half of the span only. Hence, structures rotating counter-clockwise ($\omega_x > 0$) become dark and structures rotating clockwise become bright.

With the help of Fig. 6, three theoretically known vortex structures are identified, i.e. the *passage vortex*, the *corner vortex*, and the *concentrated shed vortex*. The artifacts in the vicinity of the corner separation and the trailing edge are related to the

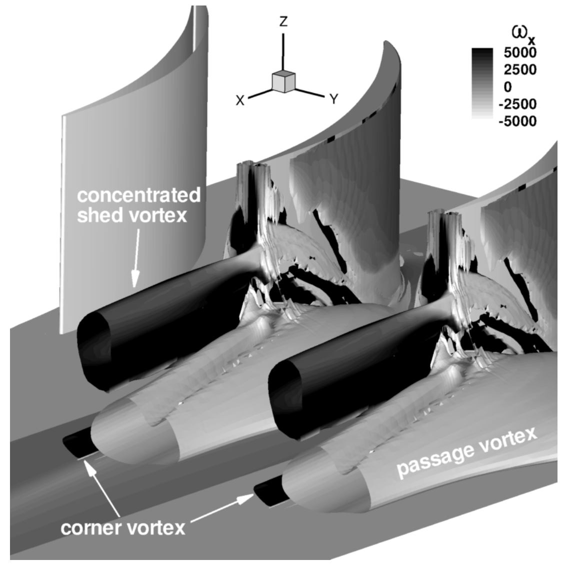


**FIGURE 6**. VISUALIZATION OF VORTEX STRUCTURES FOR THE BASE FLOW WITH THE HELP OF $\lambda_2 = -10^7$-ISOSURFACES.

definition of $\lambda_2$. Due to the analysis of the velocity gradients, the criterion is very sensitive toward velocity fluctuations occuring in these areas. All in all, it can be seen that the flow through the passage is dominated by secondary flow structures.

The resulting total pressure loss coefficient $\zeta_{q_1}$ is depicted in Fig. 7(a) on the outlet evaluation plane for the simulation and the experiment. Due to nearly symmetrical experimental results, better perceptibility is achieved by showing the data over the half span only, even though it is measured over the full span. For the simulation, the highest values of $\zeta_{q_1}$ are found at approximately 5% span and 10% pitch, as well as 20% span and 25% pitch. With the help of the three-dimensional flow field it is found that these areas of high losses are caused by the interaction of the vortex structures. In the areas between the passage vortex and the corner vortex on the one side and the shed vortex on the other side, the shear velocity is high because of the counter-rotating vortices. These areas comprise the highest losses. In the experiment, the data starts at 2.5% span since a measurement less than $1 \cdot 10^{-3}$m away from the wall is impossible. At the periodic boundaries, the extent of the losses in span-wise direction agrees very well. At mid-span, where no secondary flow effect is observed, the losses are caused by the profile itself. The profile losses are overestimated by the flow solver with an extent of approximately 19% pitch whilst in the experiment an extent of only 16% pitch is observed. Another slight discrepancy is found for the location of the highest losses. In the experiment they are located at around 15% span, whilst the simulation predicts them around 20% span. All in all, the agreement still is very good and the numerics seem able to capture the basic structure of the secondary flow as well as the resulting losses in total pressure.

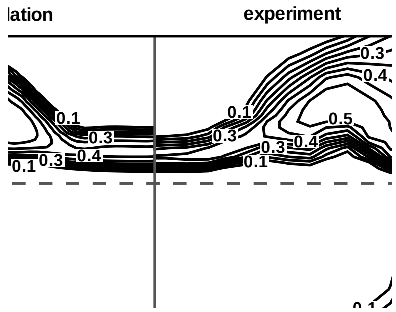


(a) LOCAL TOTAL PRESSURE LOSS COEFFICIENT ON EVALUATION PLANE.

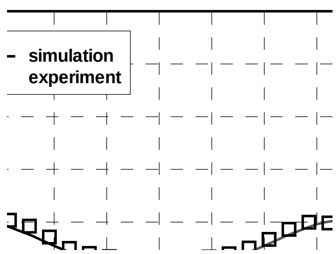


(b) SPAN-WISE DISTRIBUTION OF PITCH-AVERAGED TOTAL PRESSURE LOSS COEFFICIENT.

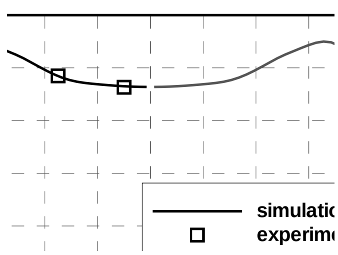

(c) SPAN-WISE DISTRIBUTION OF PITCH-AVERAGED OUTFLOW ANGLE.

**FIGURE 7**. EVALUATION OF THE UNFORCED BASE FLOW FOR SIMULATION AND EXPERIMENT.

The concurrence between simulation and experiment is fortified regarding the span-wide distribution of the pitch-averaged values of total pressure loss $\zeta_{q_1}$ and outflow angle $\alpha_2$ depicted in Fig. 7(b) and (c), respectively. In both cases, the numerical result is mirrored at mid-span even though the outflow angle is only measured for one half of the span at four distinct points. The mass-averaged distribution of the total pressure loss $\zeta_{q_1}$ (Fig 7(b)) shows that the fundamental characteristics of the complex flow field are well captured by the simulation. The slight overestimation of the profile losses at midspan is only marginally visible. Between 20% and 30% span, a minor difference is observed. Even though the simultion predicts the higher losses in this region, the mass-averaged values of the experiment are higher. Hence, there must be a deviation in mass flow. The really distinct discrepancies are found close to the wall for 10% span and less. Here, the simulation clearly overestimates the losses by up to 20%. The reason may be differences in the incoming boundary layer, variations in the location and extent of the vortex structures, discrepancies in mass flow distribution, and, last but not least, numerical and measurement uncertainties.

The prediction of the outflow angle $\alpha_2$ (Fig 7(c)) on the oher hand matches the data available from the experiment perfectly. The immense over-turning of up to $-7°$ next to the wall is related to the pressure gradient resulting from the blade camber causing a higher flow turning of the fluid within the decelerated boundary layer. Due to the limited number of conrad probes, this over-turning is not measured in the experiment and can thus not be validated. Because of the secondary flow, the design deflection of $\Delta\alpha = 42°$ is not achieved at any span-wise location more than 5% away from the wall. The span-wise distribution of the outflow angle is related to the vortex structures. Passage vortex and concentrated shed vortex cause a strong under-turning between 10% and 30% span, observed by both simulation and experiment, which diminishes toward midspan.

The relation between the vortex structures and the total pressure loss distribution is shown in Fig. 8. On the evaluation plane, the distribution of the total pressure loss coefficient is indicated by the solid isolines using the same levels as in

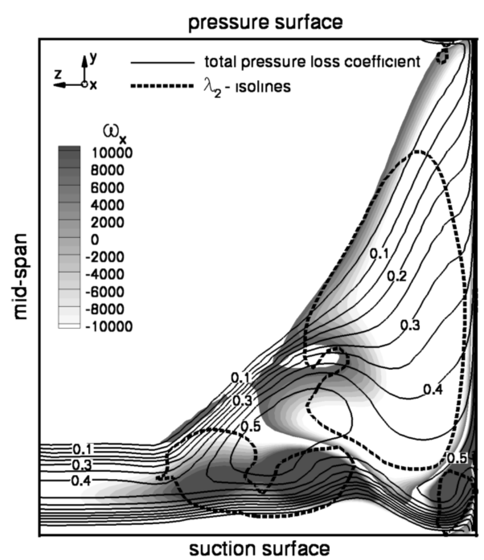


**FIGURE 8**. EVALUATION PLANE OF THE BASE FLOW SIMULATION RELATING TOTAL PRESSURE LOSS COEFFICIENT, AXIAL VORTICITY, AND THE VORTEX STRUCTURES.

**TABLE 2**. EVALUATION OF INTEGRAL AVERAGED VALUES FOR BASE FLOW CASE.

| | $\zeta_{q_1}$ [%] | $\alpha_2$ [°] | $\Delta p/q_1$ [-] |
|---|---|---|---|
| simulation | 9.2 | 8.4 | 0.385 |
| experiment | 9.0 | 8.2 | 0.355 |

Fig. 7(a). Additionally, the previously shown vortex structure is depicted by means of the dashed $\lambda_2 = -10^7$-isolines. The color contour shows the axial vorticity $\omega_x$, where values from $-3000 1/s \leq \omega_x \leq 3000 1/s$ are blanked. It can be seen that the shape of the vorticity and the vortex structures concur well. As said above, the highest values of the total pressure loss are found in the areas between the vortices, even though the corner vortex overlaps most of the small region next to the wall.

By integrating the pitch-averaged parameters, global values of the cascade performance can be given. They are summarized for the simulation and the experiment in Tab. 2 and show that the simulation slightly over-predicts all three parameters, but especially the static pressure rise. All in all, the results of the base flow simulation still are very satisfying considering the fact that a steady RANS simulation is performed.

## Forced Flow

**Numerical realization of secondary flow suction**

Secondary flow suction is numerically realized by redefining the appropriate wall-cells as inflow-segments with negative velocity in wall-normal direction. Hereby, the desired suction ratio is achieved using an average density over the slot area to calculate the according velocity applied as boundary condition at the slot inflow segments.

Even though this approach simplifies the experimental setup where the flow suction is realized via tubes connected to the plenum at the wall, it allows easy implementation within the code, and thus represents an industrial approach realizable within an everyday design process. A more complex approach with flow suction through a numerically resolved cavity is investigated as well. It will be shown that both approaches lead to very similar results. Simulations including the whole experimental setup, i.e. the plenum, are impracticable from an industrial point of view since the plenum flow is as hard to handle as the cascade flow itself. The resolved cavity is attached to the main computational domain as shown in Fig. 9.

For the forced flow cases, the performance parameters of the cascade, i.e. the total pressure loss coeficient, the static pressure rise, and the outflow angle, are related to the base fow case without suction. Thus, the discrepancies of the base flow case between simulation and experiment are neglected by giving per-

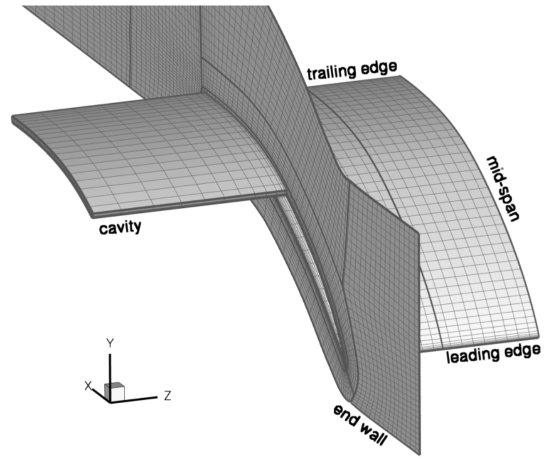


**FIGURE 9**. COMPUTATIONAL DOMAIN WITH RESOLVED CAVITY ATTACHED SHOWING ONLY EVERY SECOND GRID CELL ON THE BLADE SURACES, THE END WALL, AND THE CAVITY BLOCK.

centaged values of the performance improvement. The relative parameters are calculated as follows:

$$\Delta\Phi\ [\%] = \frac{\Phi_{suct} - \Phi_{base}}{\Phi_{base}} \cdot 100\ , \tag{3}$$

where $\Phi$ represents the performance parameter and the subscripts "suct" and "base" indicate the case with and without suction.

The drawn mass flow is related to the mass flow through the passage and given as a percentaged suction ratio $r$:

$$r\ [\%] = \frac{\dot{m}_{suct}}{\dot{m}_{passage}} \cdot 100 \tag{4}$$

**Evaluation of forced flow simulations**

At first, the two secondary flow suction approaches are evaluated by comparing the forced flow simulations against experimental data. The suction slot hereby investigated follows the design of Peacock [13] and is located in the end wall next to the suction surface of the vane. The slot extends from 50% to 100% chord in axial direction along the profile and thus covers the whole back flow area on the suction surface. The slot has a height of $0.64 \cdot 10^{-3}$m (i.e. 1.6% chord) in direction normal to the blade. Various suction ratios are considered.

Integral averaged values for the forced flow cases with various suction ratios are depicted in Fig. 10. For the total pressure loss coefficient in Fig. 10(a) and the static pressure rise in Fig. 10(b), the results of the two numerical approaches pursued are identical except of the case with a suction rate below 1%,

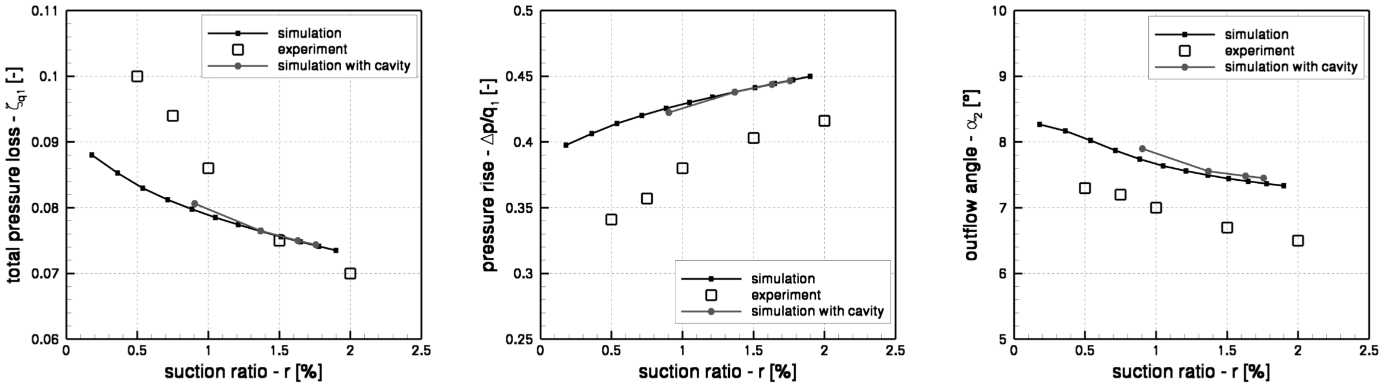


(a) TOTAL PRESSURE LOSS COEFFICIENT. (b) STATIC PRESSURE RISE. (c) OUTFLOW ANGLE.

**FIGURE 10**. EVALUATION OF VARIOUS SUCTION RATIOS THROUGH SLOT NEXT TO THE BLADE.

where the simulation resolving the cavity predicts slightly lower performance improvements. Compared to the experimental observations, the simulation massively over-predicts the impact of the flow suction for all cases with a suction ratio of up to 1%. Whilst in the numerics a performance improvement is predicted for all suction ratios investigated, the losses increase in the experiment for suction ratios below 1% and, for a suction ratio of $r = 0.5\%$, even the pressure rise is diminished. For higher suction ratios above 1.5%, the agreement between simulation and experiment is better and the differences lie in an acceptable order of magnitude. Another situation is found for the outflow angle in Fig. 10(c). Here, the simulation resolving the cavity predicts higher values than the simulation with the suction defined directly at the wall for all suction ratios. Still, the improvement is continuously lower than in the experiment where the outflow angle is at least 10% smaller than in the base flow case, even for the smallest suction ratio of $r = 0.5\%$.

The beneficial effects on all three parameters scale with the magnitude of the suction ratio. This trend is equally captured by both numerical approaches which fortifies the assumption that, for suction, resolving the cavity or defining the suction directly at the wall has no large impact. In order to really improve the predictions of the simulation, one may have to resolve the whole plenum geometry used in the experiment. The authors assume that the flow within the plenum is the reason for the massive discrepancies when it comes to small suction ratios. Whilst the velocity distribution within the slot is uniform for the case where the suction is defined directly at the wall, resolving the cavity by means of a quasi two-dimensional slot as it has been done here does lead to a non-uniform velocity distribution.

Regarding the outcome of the simulations it becomes obvious that the hereby achieved velocity distributions do still not represent the ones from the experiment. Even though the simulations with cavity lack further investigation of lower suction ratios, the trend reflected is the same as for the simple approach defining the suction at the end wall. Without resolving the cavity, computational time can be saved, variations of slot positions or geometries can be more easily investigated, and the convergence is more stable. This finding represents an important first step which enables an easy optimization of flow suction concepts using an industrial RANS approach.

For quantitative comparison between simulation and experiment, the integral averaged values for three suction ratios above 1% and the base flow case are summarized in Tab. 3. For the two higher suction ratios the simulation predicts the relative improvement in good agreement with the experiment. But the case with 1% suction is already massively over-estimated by the ideal assumption of a perfectly uniform distribution of the velocity within the slot.

**TABLE 3**. INTEGRAL AVERAGED VALUES OF FORCED FLOW CASES FOR VARIOUS SUCTION RATIOS.

| $\dot{m}_{suct}$ [%] | $\zeta_{q_1}$ [%] | $\Delta\zeta_{q_1}$ [%] | $\Delta p/q_1$ [-] | $\Delta(\Delta p/q_1)$ [%] |
|---|---|---|---|---|
| | | simulation | | |
| 0 (base) | 9.2 | ±0 | 0.385 | ±0 |
| 1.0 | 8.1 | -12.7 | 0.423 | 10.1 |
| 1.5 | 7.7 | -16.6 | 0.437 | 13.6 |
| 2.0 | 7.5 | -19.1 | 0.446 | 16.0 |
| | | experiment | | |
| 0 (base) | 9.0 | ±0 | 0.355 | ±0 |
| 1.0 | 8.6 | -4.4 | 0.380 | 7.0 |
| 1.5 | 7.5 | -16.7 | 0.403 | 13.5 |
| 2.0 | 7.0 | -22.2 | 0.416 | 17.2 |

A more detailed evaluation of the forced flow case is exemplarily shown for a suction ratio of $r = 1.5\%$ in Fig. 11. The distribution of the total pressure loss coefficient $\zeta_{q_1}$ is depicted in Fig. 11(a) for the simulation on the left and the experiment on the right side. The overall agreement is acceptable, though not as good as for the base flow case. The profile losses at midspan still match very well. Compared to the above discussed base flow case, the highest values found are reduced by 10% and the region with the highest losses is shifted toward the end wall. In the simulation, this region extends form 0% to approximately 22% span which is similar to the extent observed in the experiment. Greater discrepancy is found at around 27% span, where the simulation predicts a kink in the distribution of the losses which is not found in the measurement. From that position in direction to the wall, the extent of the calculated losses in pitch-wise direction is slightly overestimated compared to the experiment. Thus, the span-wise extension at the periodic boundaries is larger in the simulation.

The pitch-averaged distribution of $\zeta_{q_1}$ along the span (cf. Fig. 11(b)) confirms the good agreement of the profile losses at midspan. As for the base flow case, the losses in the vicinity of the end wall are over-predicted by the simulation. Another discrepancy is found between 20% and 30% span, where the numerical prediction does not follow the trend of the measurement which is related to the kink already observed in the contour plot. For comparative reasons, the result of the base flow simulation is also shown by the dashed line. It can be observed, that flow suction reduces the losses next to the wall (boundary layer losses) and between 15% and 35% span (secondary flow losses) whilst the profile losses at midspan remain unchanged.

Comparison of the pitch-averaged outflow angle $\alpha_2$, is illustrated in Fig. 11(c). The under-turning at the first two measurement points next to the wall is well predicted by the simulation. But the following decay of the outflow angle observed in the experiment with the third probe at 33% span is not visible in the numerical result. The calculated flow angle is 2.5° higher than the measured one. Again, this deviance implies differences in the secondary flow structures around that span-wise postion, related to the above described discrepancies in total pressure loss. At the mid-span nearest position, the outflow angles of simulation and experiment are in acceptable agreement. Compared to the result of the base flow simulation (dashed line), it can be seen that flow suction improves the outflow angle between 10% and 40% span.

Since no flow field measurements are available, neither within the passage not inside the plenum, the reason of the predicted kink at around 30% span can not be further evaluated. It seems that the mismatch in outflow angle relates to the differences in total pressure loss since they occur at around the same span-wise position. A possible explanation is the uniform velocity distribution in the slot assumed in the simulation. Additionally, the real geometrical slot in the end wall may cause flow separation, disturbances, or vortex structures in the experiment.

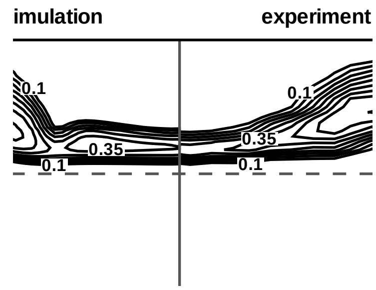


(a) LOCAL TOTAL PRESSURE LOSS COEFFICIENT ON EVALUATION PLANE.

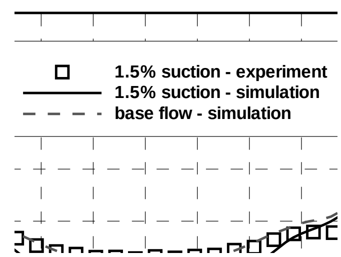


(b) SPAN-WISE DISTRIBUTION OF PITCH-AVERAGED TOTAL PRESSURE LOSS COEFFICIENT.

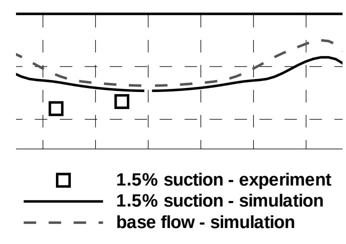


(c) SPAN-WISE DISTRIBUTION OF PITCH-AVERAGED OUTFLOW ANGLE.

**FIGURE 11**. EVALUATION OF FORCED FLOW WITH 1.5% SUCTION RATIO THROUGH SLOT NEXT TO THE BLADE.

But the differences are in an acceptable order of magnitude with respect to the RANS approach trying to resolve the complex flow structures involved. This is not obvious since linear eddy viscosity models only capture the first order effects of the Reynolds stress anisotropy and streamline curvatures which are strongly pronounced in secondary flow fields. All in all, within a simple industrial RANS approach, the simulation is able to determine the impact of secondary flow suction and predicts the trends observed in the experiment.

### Variation of suction slot position

With respect to the satisfying predictions of the forced flow simulations in comparison to the measurement, the position of the suction slot is varied numerically in the following. An offset from the blade in pitch-wise direction normal to the suction surface is investigated in two steps. One offset follows the observations from Gbadebo et al. [21] who found that a slot approximately 2% of the span away from the suction side being more effective than a slot directly at the blade. Here, that instruction leads to an offset of 0.8mm. With 2.0mm, the second offset-slot considered is more than twice as far away from the blade. The three slots investigated run from 50% – 100% chord and have a height of $0.64 \cdot 10^{-3}$m. For each slot three suction ratios are analysed, i.e. 0.5%, 1.0%, and 1.5% of the passage mass flow. The impact of the flow suction at different pitch-wise positions is evaluated by means of the relative integral averaged values, illustrated in Fig. 12. First, it can be seen that the performance of the cascade increases with rising suction ratio for the slot directly at the blade and the 0.8mm offset-slot. Regarding the 2.0mm offset-slot, the achieved reduction in total pressure loss and the gain in pressure rise remain nearly constant with varying suction ratio. The 2.0mm offset-slot performs worst. According to the observations from Gbadebo et al. [21], positioning of the slot 0.8mm away from the blade results in slightly better performance values than achieved with the slot directly at the vane.

This observation is related to the flow structure within the passage. Due to the pressure gradient between pressure side of one blade and suction side of an adjacent blade, a flow structure along the end wall develops from the pressure toward the suction side (cf. Fig. 6). This flow structure hits the suction surface and causes the corner separation. If the suction slot is located too far away from the blade and too far downstream, this phenomena takes place nearly undisturbed. On the other hand, if the slot is located close to the blade but not directly at the suction surface, most of the flow coming from the pressure side along the end wall can be sucked off, whilst the slot is still located within the separated region related to the corner stall.

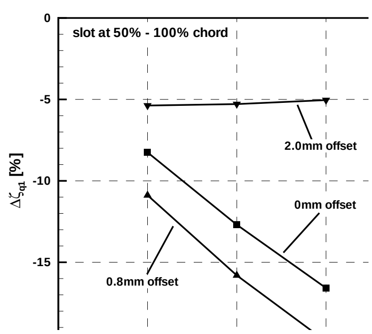


(a) TOTAL PRESSURE LOSS.

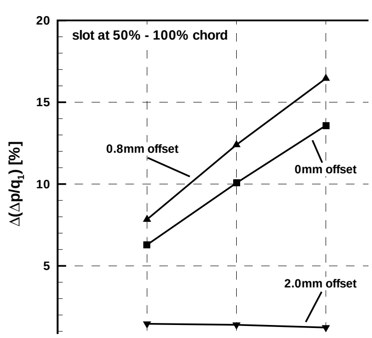


(b) PRESSURE RISE.

**FIGURE 12**. RELATIVE INTEGRAL AVERAGED VALUES WITH RESPECT TO BASE FLOW FOR VARIATION OF SUCTION RATIO THROUGH SLOTS FROM 50%–100% CHORD AT THREE DIFFERENT DISTANCES FROM THE SUCTION SURFACE.

## CONCLUSION

Numerical and experimental investigations of a high-speed 3D linear compressor cascade with steady secondary flow suction are presented. Analysis of the base flow reveals a strong corner separation next to the suction surface trailing edge. The three-dimensional flow field of the simulation shows a relation between the regions of highest losses and the interaction between counter-rotating flow structures dominating the passage.

The overall agreement between simulation and experiment is satisfying with respect to an industrial RANS approach. The complex three-dimensional flow field is well predicted, even though linear eddy viscosity models only capture the first order effects of the Reynolds stress anisotropy and streamline curvatures which are strongly pronounced in secondary flow fields. Discrepancies in total pressure loss coefficient analysis next to the wall are related to uncertainties of the incoming flow.

Secondary flow suction through slots in the end walls is considered. Following the design of Peacock [13], the geometry under investigation is located in the corner between suction side and end wall. Different suction ratios are simulated and compared against experimental data. Whilst the agreement is acceptable for higher suction ratios, the simulation is unable to capture the secondary flow effects arising in the experiment due to a plenum chamber attached to the end walls in order to realize the flow suction. Resolving the cavity by a simple quasi two-dimensional domain results in the same over-prediction as the definition of the suction directly at the end wall. It is assumed that the impact of the flow suction, especially for lower suction ratios, strongly depends on the realization of the suction process in the experimental setup. Thus, ongoing numerical investigations consider different approaches to resolve the cavity by means of nozzles or diffusors. Since the accordance between simulation and experiment is adequate for higher suction ratios, the suction flow seems to become more uniform in the experiment with rising suction mass flow. Overall, the flow solver is able to predict the impact of the forced flow and well captures the trends in compressor performance with varying suction ratio.

A numerical variation of the slot position is performed. The slot is offset away from the blade in pitch-wise direction normal to the suction surface. The simulations show that a slot close to the blade performs slightly better than the slot directly in the corner, since the secondary flow from the adjacent blade's pressure side can be removed more effectively. This benefit exists only if the slot is close enough to the blade to efficiently suck off the secondary flow from the corner stall.

The work presented shows the feasibility of predicting the impact of secondary flow suction by means of steady RANS simulations. The results show that the impact of the secondary flow suction is mainly driven by the magnitude of the drawn mass flow. The boundary conditions at the inlet of the cascade and for the realization of the suction play an important role in order to achieve good agreement with experimental data. Beneficial control locations can be determined numerically.

## ACKNOWLEDGMENT

The work presented in this paper is part of a project funded by the German Science Foundation (DFG). The authors are grateful for the support.

## REFERENCES

[1] Wennerstrom, A.J., 1990. "Highly Loaded Axial Flow Compressors: History and Current Developments". *ASME Journal of Turbomachinery,* ***112***, pp. 567–578.

[2] Gallimore, S.J., Bolger, J.J., Cumpsty, N.A., Taylor, M.J., Wright, P.I., and Place, J.M.M., 2002. "The Use of Sweep and Dihedral in Multistage Axial Flow Compressor Blading–Part I and II". *ASME Journal of Turbomachinery,* ***124***, pp. 521–542.

[3] Staubach, J.B., Sharma, O.P., and Stetson, G.M., 1996. "Reduction of Tip Clearance Losses Through 3-D Airfoil Designs". *IGTI 96-TA-013*.

[4] Hergt, A., Meyer, R., and Engel, K., 2006. "Experimental Investigation of Flow Control in Compressor Cascades". *ASME GT2006-90415*.

[5] Lord, W.K., MacMartin, D.G., and Tillman, G., 2000. "Flow Control Opportunities in Gas Turbine Engines". *AIAA 2000-2234*.

[6] Herzig, H. Z., Hansen, A. G., and Costello, G. R., 1953. "A Visualization Study of Secondary Flows in Cascades". *NACA Technical Report 1163*.

[7] Schlichting, H., 1957. "Cascade Flow Problems". *AGARD Report 93*.

[8] Horlock, J. H., Luis, J. F., Percival, P. M. E., and Lakshminarayana, B., 1966. "Wall Stall in Compressor Cascades". *Journal of Basic Engineering, ASME*.

[9] Kang, S., and Hirsch, C., 1991. "Three Dimensional Flow in a Linear Compressor Cascade at Design Conditions". *ASME 91-GT-114*.

[10] Gbadebo, S. A., Cumpsty, N. A., and Hynes, T.P., 2005. "Three-Dimensional Separations in Axial Compressors". *ASME Journal of Turbomachinery,* ***127***.

[11] Sinnettej, T., and Costello, G. R., 1951. "Possible Application of Blade Boundary-Layer Control to Improvement of Design and Off-Design Performance of Axial-Flow Turbomachines". *NACA Technical Note 2371*.

[12] Costello, G. R., Cummings R. L., and Serovy, G. K., 1952. "Experimental Investigation of Axial-Flow Compressor Stator Blades Designed to obtain High Turning by means of Boundary-Layer Suction". *NACA RM E52D18*.

[13] Peacock, R. E., 1965. "Boundary-Layer Suction to Eliminate Corner Separation in Cascades of Airfoils". *University Engineering Department, Cambridge, Reports and Memoranda No. 3663*.

[14] Liesner, K., Meyer, R., Lemke, M., Gmelin, C., and Thiele, F., 2010. "On the Efficiency of Secondary Flow Suction in a Compressor Cascade". *ASME GT2010-22336*.

[15] Liesner, K., and Meyer, R., 2008. "Experimental Setup for Detailed Secondary Flow Investigation by Two-Dimensional Measurement of Total Pressure Loss Coefficients in Compressor Cascades". *VKI XIX Symposium on Measurement Techniques in Turbomachinery, Sint Genesius-Rhode, Belgium*.

[16] Xue, L., 1998. "Entwicklung eines effizienten parallelen Lösungsalgorithmus zur dreidimensionalen Simulation komplexer Strömungen". *Ph.D. Thesis, Technische Universität Berlin*.

[17] Weber, A., 2008. *G3DMESH v4.5.4*. DLR, Institut für Antriebstechnik, Köln.

[18] Lien, F., and Leschziner, M., 1994. "A general non-orthogonal collocated finite volume algorithm for turbulent flow at all speeds incorporating second-moment turbulence-transport closure, Part 1: Computational Implementation". *Comput. Meth. Appl. Mech. Eng.,* ***114***, pp. 123–148.

[19] Menter, F., 1992. "Performance of popular turbulence models for attached and separated adverse pressure gradient flows". *AIAA Journal,* ***30***(8), pp. 2066–2072.

[20] Jeong J,, and Hussain F., 1995. "On the identification of a vortex". *JFM,* ***285***.

[21] Gbadebo, S. A., Cumpsty, N. A., and Hynes, T.P., 2008. "Control of Three-Dimensional Separations in Axial Compresors by Tailored Boundary Layer Suction". *ASME Journal of Turbomachinery,* ***130***.